

Structural instability and charge transfer mediated transition in $\text{Pr}_3\text{Co}_4\text{Sn}_{13}$: A synchrotron radiation based scattering and spectroscopic study

Surajit Ghosh^{1,*}, Chin-Wei Li^{1,*}, Chih-En Hsu¹, Yu-Hui Liang¹, Wei-Xuan Lin¹, Kuan-Hung Chen¹, Hsio-Tsu Wang^{1,2},
Chao-Hung Du¹, Jau-Wern Chiou^{3,†}, Huang-Ming Tsai⁴, Jeng-Lung Chen⁴, Chih-Wen Pao⁴, Cheng-Maw Cheng⁴,
Chia-Nung Kuo^{5,6}, Chin-Shan Lue^{5,6}, Sekhar Chandra Ray^{7,8}, Hung-Chung Hsueh^{1,‡} and Way-Faung Pong^{1,§}

¹*Department of Physics, Tamkang University, New Taipei City 251, Taiwan*

²*Bachelor's Program in Advanced Materials Science, Tamkang University, New Taipei City 251, Taiwan*

³*Department of Applied Physics, National University of Kaohsiung, Kaohsiung 811, Taiwan*


⁴*National Synchrotron Radiation Research Center, Hsinchu 300, Taiwan*

⁵*Department of Physics, National Cheng Kung University, Tainan 701, Taiwan*

⁶*Taiwan Consortium of Emergent Crystalline Materials, National Science and Technology Council, Taipei 106, Taiwan*

⁷*Department of Physics, ITER, Siksha 'O' Anusandhan, Deemed to be University, Bhubaneswar 751 030, Odisha, India*

⁸*Department of Physics, CSET, University of South Africa, Florida Park 1710, Johannesburg, South Africa*

 (Received 23 July 2024; revised 21 February 2025; accepted 17 March 2025; published 11 April 2025)

This study aims to clarify the physics of the transition that is observed in $\text{Pr}_3\text{Co}_4\text{Sn}_{13}$ (PCS) by specific heat at ~ 138 K, which resembles the formation of a charge density wave (CDW). The work is performed using synchrotron radiation based scattering and spectroscopic techniques that include temperature-dependent x-ray diffraction (XRD), x-ray scattering (XRS), x-ray absorption near-edge structure (XANES)/extended x-ray absorption fine structure (EXAFS), resonant inelastic x-ray spectroscopy (RIXS), valence-band photoemission (VB-PES), and first-principles calculation. The appearance of satellite features in the XRD and XRS studies revealed a modulation of the structure along a new \mathbf{q} vector (0.5,0.5,0) below 120 K. Phonon calculations suggest softening of a phonon mode and a possible superlattice transition at low temperatures. The XANES spectra of the Sn K , Co $L_{3,2}$, and Pr $M_{5,4}$ edge revealed an increase of charge transfer (CT) at low temperatures as a result of an enhancement of Co $3d$ -Sn $5p$ /Pr $4f$, and Pr $4f$ -Sn $5p$ hybridizations. The EXAFS study at the Sn K edge further suggested local distortion of the Sn sites because of Sn-Sn bond elongation at low temperatures. The VB-PES study and theoretical calculations that are based on spin-polarized density functional theory together confirm the strength of hybridization and the lack of any significant change in the band gap of the PCS with temperatures. The RIXS spectra at the Co L_3 edge provide further evidence of the CT process, and the energy level of Co $3d$ states below the Fermi level were found to be static in the temperature range of 80 to 300 K, implying no change in the band gap of the PCS with temperatures. Based on the relevant results, the appearance of a clear kink around 138 K in the temperature-dependent specific heat measurements is caused by local lattice distortion at the Sn sites by a diffusionless mechanism, resulting in minimal alteration of the electronic structure through Sn-Sn bond elongation and widening of the Sn-Co-Sn bond angle in PCS. Thus, this study suggests that the system does not undergo a CDW transformation unlike many other similar materials.

DOI: [10.1103/PhysRevB.111.165119](https://doi.org/10.1103/PhysRevB.111.165119)

I. INTRODUCTION

Low-dimensional materials that consist of transition metals (TM) and rare-earth (RE) elements have emerged as promising platforms for the study of intriguing topological and electronic states. Understanding the strong correlation between TM d and RE f electrons in these systems has become an important goal of researchers in condensed matter physics. These materials are technologically significant because they will have a wide range of applications in the future [1,2]. Along with

the strongly correlated electrons, structural distortions are key features of these materials, which play a critical role in various exotic electronic effects, such as the heavy fermion phenomenon, the Kondo effect, complicated magnetism, charge density wave (CDW) formation and superconductivity, among others [3–15]. A CDW involves correlated states that are usually associated with the periodic distortion of the lattice, resulting in the formation of a wavelike pattern of charge density and modulation of the Fermi surface (FS) of the system [16,17]. The formation of a CDW has been explained with reference to FS nesting and/or strong electron-phonon coupling [18–20]. There are many arguments regarding whether FS nesting, which is a purely electronic effect that has been found to favor CDW formation, is or is not the sole driving force of CDW formation [17,21]. The electronic instabilities of CDWs have been shown to be easily destroyed by

*These authors contributed equally to this work.

†Contact author: jwchiou@nuk.edu.tw

‡Contact author: hchsueh@gms.tku.edu.tw

§Contact author: wfpong@mail.tku.edu.tw

even a small deviation from the perfect FS nesting condition [17,21,22]. However, lattice distortion is a necessary but insufficient condition for the formation of a CDW [17]. Thus, identifying and analyzing CDW modulation have been difficult tasks that have attracted researchers since Pierls proposed the phenomenon in one-dimensional (1D) materials [16]. Quasi-1D materials, such as NbSe₃, were the first to be used to study CDW formation, which was initially believed to be a 1D phenomenon only [19,20,22]. Later, CDWs were found in quasi-two-dimensional (2D) and three-dimensional (3D) materials, including 2D TM chalcogenides and 3D RE oxides [7,9,12,14,15,23,24].

Single-crystal ternary stannide materials ($RE_3TM_4Sn_{13}$), which are well known for exhibiting superconductivity around 10 K, yield anomalous specific heat (C_p), resistivity (ρ), and magnetization measurements between 120 and 170 K, commonly attributed to the CDW transition, making them platforms for the study of 3D CDW transitions. Structural distortion that is associated with the trigonal symmetry of materials has a crucial role in the formation of CDW-like transitions. The CDW-like transition or modulation is followed by the formation of a superlattice (by a cell-doubling transformation of the structure) [7–12,14]. However, the origin of the phase transition is controversial, as is the question of whether the superlattice formation is related to the CDW transition in the $RE_3TM_4Sn_{13}$ structure [11–15]. Additionally, $Sr_3Ir_4Sn_{13}$ and $Sr_3Rh_4Sn_{13}$ exhibit CDW instability below 147 and 138 K, respectively, at the Sn sites, and the CDW transitions are accompanied by a cell-doubling structural transition with the generation of a new q vector in the (0.5,0.5,0) direction [11,12]. The formation of this new q vector below the CDW transition temperature has been regarded as evidence of the presence of a CDW in many materials [7–9,11–14]. $Ce_3Co_4Sn_{13}$ has been determined to form a CDW ($T = 160$ K) by the making of C_p measurements and through nuclear magnetic resonance studies, this phenomenon is associated with heavy fermion behavior at the same temperature [7,15]. In contrast, Otomo *et al.* have shown that a single-crystal sample of $Ce_3Co_4Sn_{13}$ that was grown by the Sn flux method undergoes a cell-doubling structural transition (superlattice formation) without a CDW transition [13]. Accordingly, earlier reports on similar materials with superlattice formation have in some cases supported and in other cases not supported the fact of CDW transition, making the identification of CDW and superlattice formation in such systems difficult. Interestingly, the hybridization between Co d and Sn p states in $Ce_3Co_4Sn_{13}$ has been highlighted, but RE f electrons have been found not to play any role in the phase transition, and the conduction-band edge of these materials is thought to be formed primarily by Co $3d$ and Sn $5p$ states [15]. Theoretical band-structure calculations of $RE_3TM_4Sn_{13}$ suggest strong hybridization of TM $3d$ and Sn $5p$ states within the $TM(Sn)_6$ trigonal prism, which lie at/near the Fermi level (E_F) of the system [25]. The relevance of the correlation among TM d , Sn p , and RE f electronic states to the CDW transition deserves more attention. The question of whether, in these structures, superlattice formation is inextricably related to the CDW transition must be addressed. Although a study on single-crystal $Pr_3Co_4Sn_{13}$ (PCS) has predicted CDW-like transitions in materials, based on C_p and nuclear magnetic res-

onance studies at ~ 138 K [26], no concrete evidence to prove that has been published yet. To the best of our knowledge, no work has been done to determine the local electronic and atomic structures of PCS using x-ray scattering (XRS) and related spectroscopic techniques with a view to understanding CDW transition. In this study, temperature-dependent x-ray diffraction (XRD), XRS, x-ray absorption near-edge structure (XANES)/extended x-ray absorption fine structure (EXAFS), resonant inelastic x-ray scattering (RIXS), and valence-band photoemission spectroscopy (VB-PES) were performed on a single-crystal PCS system, and the results were supported by first-principles spin-polarized density functional theory (DFT) calculations. One key finding is that charge transfer (CT) is caused by the enhancement of Co $3d$ -Sn $5p$ /Pr $4f$ and Pr $4f$ -Sn $5p$ hybridizations and structural instability at low temperatures. These phenomena are used to explain the appearance of a clear kink at low temperatures in the C_p measurements. Our study of PCS provides a comprehensive approach to addressing the critical question of whether this compound exhibits CDW modulation. By carefully investigating its structural, electronic, and thermal properties, we establish a robust framework for analyzing the potential emergence of CDW behavior in PCS. Furthermore, our study introduces a distinctive methodology for identifying subtle signatures of CDW, enabling a deeper understanding of its absence or presence in this material. This approach not only refines the criteria for detecting CDW transitions but also underscores the uniqueness of PCS among $RE_3TM_4Sn_{13}$ compounds that commonly display such phenomena. The roles of strongly correlated Co d , Sn p , and Pr f electronic states and their hybridizations at various temperatures are investigated extensively. This study explores the relationship between structural modulation, the emergence of a new q vector in a specific direction, and the possible formation of a CDW aiming to investigate whether such phenomena are inherently linked.

II. EXPERIMENT

Temperature-dependent Co K -, $L_{3,2}$ -, Sn K -, and Pr $M_{5,4}$ -edge XANES spectra were obtained in fluorescence mode using the Taiwan Light Source (TLS) 17C, 01C, and 20A beamlines at the National Synchrotron Radiation Research Center (NSRRC), Hsinchu, Taiwan. The energy resolution for the Co (Sn) K -edge XANES measurement was set to ~ 0.5 eV (1.5 eV) at a photon energy of 7.7 keV (29.2 keV) and for the Co $L_{3,2}$ -edge (Pr $M_{5,4}$ -edge) XANES measurements was set to ~ 0.1 eV (0.1 eV) at a photon energy of 778 eV (928 eV). Co and Sn metals were used as references to calibrate the photon energy scale. The temperature-dependent high-resolution XRD patterns were recorded at the Taiwan Photon Source (TPS) 19A beamline of the NSRRC using a wavelength of 16 keV (0.774 89 Å). Temperature-dependent XRS was performed at the TLS 07A beamline. The incident x-ray energy was set to 14.0 keV (equivalent wavelength of 0.885 605 Å) using a perfect Si(111) double-crystal monochromator. The eight-circle diffractometer allowed the crystallographic axes to be aligned in reciprocal space for XRS measurement. To increase the spatial resolution, a high-quality LiF(200) crystal was used as an analyzer. Co L_3 -edge RIXS spectra of

PCS at various temperatures (80–300 K) were recorded at the TPS 45A2 TKU-endstation beamlines [27]. Temperature-dependent VB-PES spectra were obtained at the TLS 21B1 beamline with the use of a hemispherical analyzer to collect the photoelectrons, and the energy of the incident photons was set to 75.0 eV. The energy of the VB-PES spectra was calibrated using the E_F of clean gold. The zero energy refers to the valence-band maximum (E_{VBM}), which is the threshold of the emission spectrum. To make all temperature-dependent measurements, the single-crystal PCS was mounted in a closed-cycle He cryostat, with a temperature stability of approximately ± 1 K. A single crystal of PCS with an area of $\sim 2 \text{ mm} \times 4 \text{ mm}$ was grown using the Sn self-flux method, in which a high-purity starting elemental metals molar ratio of 1:1:20 was used. All experiments were conducted on pieces cut from the single large single crystal to ensure consistency in the measurements. The normal direction of the crystal was [220] as characterized by XRD using an in-house x-ray diffractometer with Cu K_α radiation [26]. The Rietveld refinement of the XRD data were performed using the FULLPROF software package [28]. Temperature-dependent C_p , ρ , and magnetic susceptibility (χ) measurements were made using a high-resolution ac calorimeter, the traditional four-point probe technique (four platinum wires), and a superconducting quantum interface device magnetometer, respectively.

First-principles calculations

Based on DFT, first-principles spin-polarization calculations were made using the projector augmented-wave method in the Vienna *ab initio* Simulation Package (VASP) [29,30] to determine the ground-state electronic structures and magnetic properties of metallic PCS. A spin-polarized generalized gradient approximation (GGA) with the Perdew-Burke-Ernzerhof functional was used to specify the electronic exchange-correlation interactions [31]. A conjugate gradients scheme was used to optimize the atomic configurations under the influence of Hellmann-Feynman forces with a tolerance of 10^{-3} eV/Å. An energy cutoff of 400 eV was used to expand the plane-wave basis set. Brillouin zone integration was performed in k -points sampling on a $16 \times 16 \times 16$ Monkhorst-Pack grid. A simplified rotationally invariant DFT+ U method, introduced by Dudarev *et al.* [32] with an effective Hubbard U parameter ($U_{\text{eff}} = 6$ eV) for both Co $3d$ and Pr $4f$ orbitals, was applied to address the correspondence to strong on-site Coulomb interactions [33–36]. Based on the calculated total energies for a 40-atom unit cell of PCS, the structural stability of the G -type-like antiferromagnetic (AFM) order of an individual Co/Pr sublattice is supported by its much lower energy ($\Delta E = -0.2$ eV/atom) than that of the ferromagnetic (FM) phase. Furthermore, the phonon band structure of PCS was derived from the calculated real-space force constants in supercells with symmetrized displacement patterns using the PHONOPY software [37]. A finite atomic displacement amplitude of 0.01 Å was used. Owing to the previous observation of structural instability in $\text{La}_3\text{Co}_4\text{Sn}_{13}$ [38] with the same crystallographic symmetry, a $2 \times 2 \times 1$ supercell of cubic PCS was constructed to calculate its lattice vibrational frequencies and the corresponding eigenvectors of its phonon modes at the point M (0.5,0.5,0).

III. RESULTS AND DISCUSSION

A. Structural and physical property study

Figure 1(a) presents the Rietveld refinement of the powder XRD pattern that was recorded using in-house Cu K_α radiation at room temperature; all features are matched to corresponding ICSD data (file No. 600231). The refinement of the XRD data reveals that PCS crystallizes with a cubic structure, in space group $Pm\bar{3}n$, as shown in the inset of Fig. 1(a), in which colors are used to more clearly visualize the constituent atoms of the crystal structure [8]. Pr is bonded in a 12-coordinate geometry to 4 equivalent Co and 12 equivalent Sn atoms and Co is bonded in a 6-coordinate geometry to 3 equivalent Pr and 6 equivalent Sn atoms. The two Sn sites in the structure are Sn₁ and Sn₂. Sn₁ is bonded in a nine-coordinate geometry to 3 equivalent Pr, 2 equivalent Co, and four Sn atoms, while Sn₂ is bonded in a cubicoctahedral geometry to 12 equivalent Sn atoms. This complex structure of the $\text{RE}_3\text{TM}_4\text{Sn}_{13}$ materials has been studied in detail elsewhere [8]. Bond lengths were estimated from the Rietveld refinement of the XRD patterns that are recorded at room temperature [Fig. 1(a)] and are listed in Table I along with their coordination numbers to elucidate the complexity of the structure. The details of refinements at 300 and 90 K are presented in the Figs. S1(a) and S1(b), respectively, in the Supplemental Material (SM) [39]. Figure 1(b) displays high-resolution XRD patterns that were recorded at temperatures from 90 to 300 K in the 2θ range $\sim 42.4^\circ$ – 53.0° . XRD patterns were recorded using a 16-keV photon source equivalent to 0.774 89 Å at the TPS 19A beamline of the NSRRC. The patterns of the 2θ range presented here are converted to in-house Cu K_α wavelength for convenience. No clear variation of the crystal structure is identified as the patterns of the powder PCS throughout the temperature range are similar. Close observation of the region [left inset in Fig. 1(b)] between the prominent peak (around $\sim 46.5^\circ$) that corresponds to the [422] plane reveals that the peak shifted toward a higher angle as the temperature decreased from 300 to 100 K. Other features are observed to have shifted to higher angles at lower temperatures, indicating a gradual decrease in the lattice parameters. The lattice parameter and the cell volume of the structure that were estimated from the XRD patterns at 300, 150, and 90 K, listed in Table II, also indicate this gradual decrease. Interestingly, below 120 K, two new features (indicated by red arrows, at $\sim 42.7^\circ$ and 43.8°) arise at a lower angle, as shown in the magnified XRD patterns in the right inset in Fig. 1(b). The new satellite features are attributed to diffraction from the (4.5,0.5,0) and (4.5,1.5,0) planes, clearly indicating modulation of the crystal structure and the formation of a new q vector following in the (0.5,0.5,0) direction in PCS at lower temperatures. In other similar materials the formation of a modulated structure with a new q vector along the same direction has been linked to a transition from a simple cubic phase ($Pm\bar{3}n$ space group) to a body-centered cubic phase ($I\bar{4}3d$ space group), with near doubling of the latter parameter [8,14]. In our case such cell-doubling transformation cannot be found conclusively. Rather, the crystal structure retains its cubic nature ($Pm\bar{3}n$), as indicated by the lattice parameters and the lack of changes in the integrated intensities of selected reflections [(400), (410), and (411)] across the transition

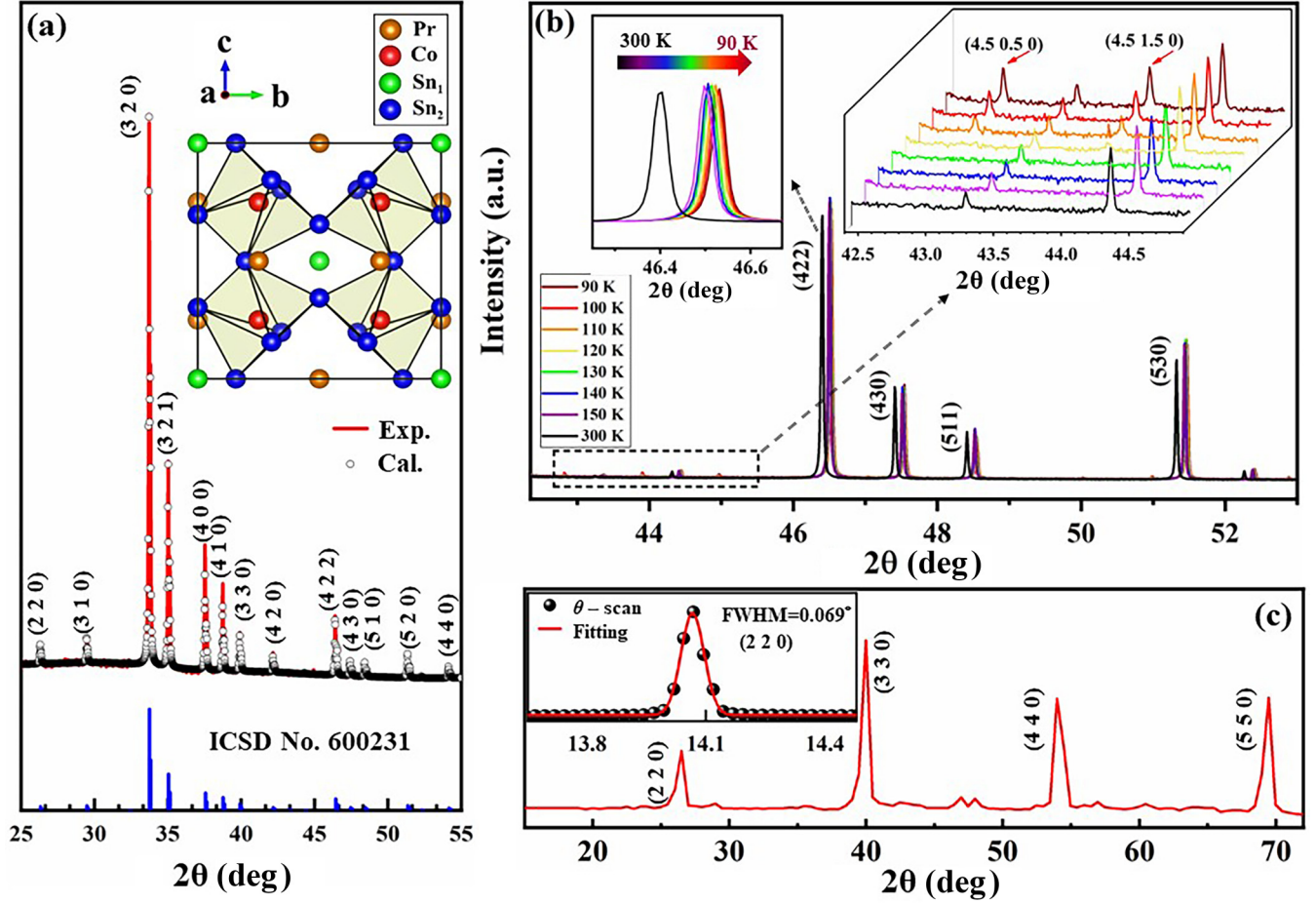


FIG. 1. (a) Rietveld refinement of the XRD pattern of powder PCS along with its structure. (b) Temperature-dependent XRD patterns. Right inset shows small-angle zoom-in in the range 42.5° – 44.9° . Left inset shows the zoom-in of the peak [422]. (c) XRD patterns of single-crystal PCS. Top inset shows XRD measurement on the (220) plane.

temperature [see Figs. S2(a) and S2(b) in the SM [39]]. In fact, The host lattice does not change across the transition temperature; instead, the unit cell of the crystal structure is doubled by the formation of the modulated structure. XRD patterns of the single-crystal PCS were also recorded at room temperature [Fig. 1(c)], and Bragg's reflection along [220], [330], [440], and [550] were clearly observed, indicating growth of the

crystal in the [110] direction. The small full width at half maxima (FWHM = 0.069°) of the observed [220] feature further confirms the high quality of the single-crystal PCS.

Figure 2 displays the temperature dependence of $C_p(T)$ that was measured on the [220] plane of the single-crystal PCS in the temperature range 80–240 K in both heating and cooling cycles. The appearance of a clear kink around a temperature of $T = 138$ K (labeled as T^*) implies a possible structural transition in the PCS. This transition is attributed to a CDW-like phase-induced structural transition and FS reconstruction in many similar materials, such as $\text{Ce}_3\text{Co}_4\text{Sn}_{13}$ and $\text{La}_3\text{Co}_4\text{Sn}_{13}$ [9,12]. However, CDW transitions are in general first-order transitions resulting in clear thermal hysteresis when measured in heating and cooling cycles. No such

TABLE I. Different bonds and their bond lengths of the PCS structure evaluated from the Rietveld refinement of the XRD data collected at 300 K.

Bond	Distance (Å) (number)
Co-Sn ₂	2.60 (3)
Co-Pr	3.38 (4)
Co-Sn ₁	4.14 (5)
Sn ₂ -Co	2.61 (3)
Sn ₂ -Pr	3.33 (4)
Sn ₂ -Pr	3.38 (4)
Sn ₂ -Sn ₁	3.30 (4)
Sn ₂ -Sn ₂	3.60 (4)
Sn ₁ -Pr	5.35 (3)

TABLE II. Lattice parameter and cell volume of PCS at various temperatures measured from XRD.

Temperature (K)	Lattice parameter (a) (Å)	Cell volume (V) (Å ³)
90	9.554 ± 0.001	872.08 ± 0.01
150	9.560 ± 0.001	873.72 ± 0.01
300	9.579 ± 0.001	878.94 ± 0.01

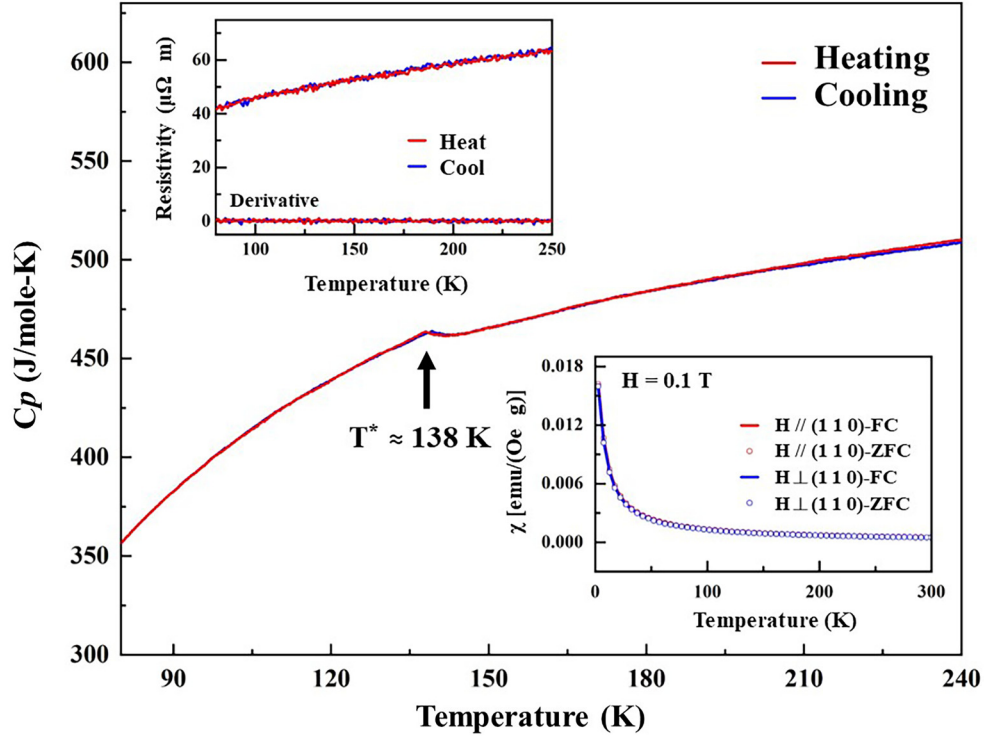


FIG. 2. Temperature dependence of C_p of single-crystal PCS. Top inset shows the temperature dependence of ρ . Bottom inset shows temperature-dependent magnetic susceptibility (χ vs T), measured in a magnetic field of 0.1 T parallel and perpendicular to (1 1 0).

clear hysteresis can be seen in the zoomed view presented in Fig. S3 in the SM. Although there is a very small hysteresis present between the two cycles, it can be neglected as it is too small (less than 1 K). The absence of convinced hysteresis in the heat capacity data indicates that the transition is likely second order in nature. On the other hand, such a transition in $RE_3TM_4Sn_{13}$ systems has also been described as a cell-doubling crystallographic transformation, owing to the small distortion at the Sn sites from their primary positions [26]. The CDW creates periodic potential modulation, causing the local electron density to exhibit a periodic variation, which affects the energy levels that are available to electrons in the compound. Notably, the periodic lattice distortion associated with the CDW can cause the electrons preferentially to occupy their lower energy states, leading to a rearrangement of the electronic structures in the compound. Furthermore, electron-electron interactions, combined with the CDW potential and coupling between the electron and phonon, lead to Peierls instability [16]. As a result of the instability, typically, the CDW preferentially opens an energy gap in the electronic band structure at/near the E_F [16–23]. The opening of the energy gap at/near the E_F due to the formation of the CDW has significant effects on the electronic and transport properties of the material, including changes in ρ and other properties, as mentioned above. The temperature-dependent ρ was measured in the temperature range 80–250 K to verify this effect. The top inset in Fig. 2 plots ρ as a function of temperature (T), revealing a monotonous increase of ρ with temperature. The measurements were performed on single-crystalline samples with the current flowing in the ab plane, focusing on the in-plane electronic behavior of the material. This configuration is appropriate for detecting resistivity changes arising from

electronic or structural transitions that influence the ab -plane conductivity. Previous studies [12,14] on materials exhibiting similar structural modulations, characterized by a modulation vector of $\mathbf{q} = (0, 0, 0.5)$, reported resistivity changes when measured along the ab plane, consistent with our experimental setup. While those studies identified resistivity anomalies associated with a CDW transition, our measurements in the ab plane show no such anomalies. Specifically, no irregularities or “kinks” were observed in the temperature-dependent resistivity $\rho(T)$ or its derivative (shown in the lower inset of Fig. 2), indicating the absence of a metal-insulator or metal-semiconductor transition. This is in contrast to the temperature-dependent C_p measurements, which reveal a distinct kink near 138 K (T^*), characteristic of the single-crystal PCS system.

To determine whether the transition at T^* in PCS originates in the spin ordering of the material, the magnetic property of the compound was studied. The bottom inset in Fig. 2 shows the variations of magnetization under field cooling and zero-field cooling (ZFC) of a single-crystal PCS in the temperature range 2–300 K in an applied magnetic field of 0.1 T measured in in-plane and out-of-plane (110) geometry. Curie-Weiss-like paramagnetic behavior was observed in the magnetization study down to 2 K. The absence of any anomaly close to the transition temperature (T^*) in specific heat measurement excludes the possibility that the transition has a magnetic/spin origin. The ZFC susceptibility data were fitted using the Curie-Weiss law [$\chi = C/(T - \theta_{CW})$], where χ is the susceptibility of the material, C is the Curie constant, and T and θ_{CW} represent the temperature and the paramagnetic Curie-Weiss temperature, respectively (see Fig. S4 in the SM). The purpose is to identify the magnetic interaction in the

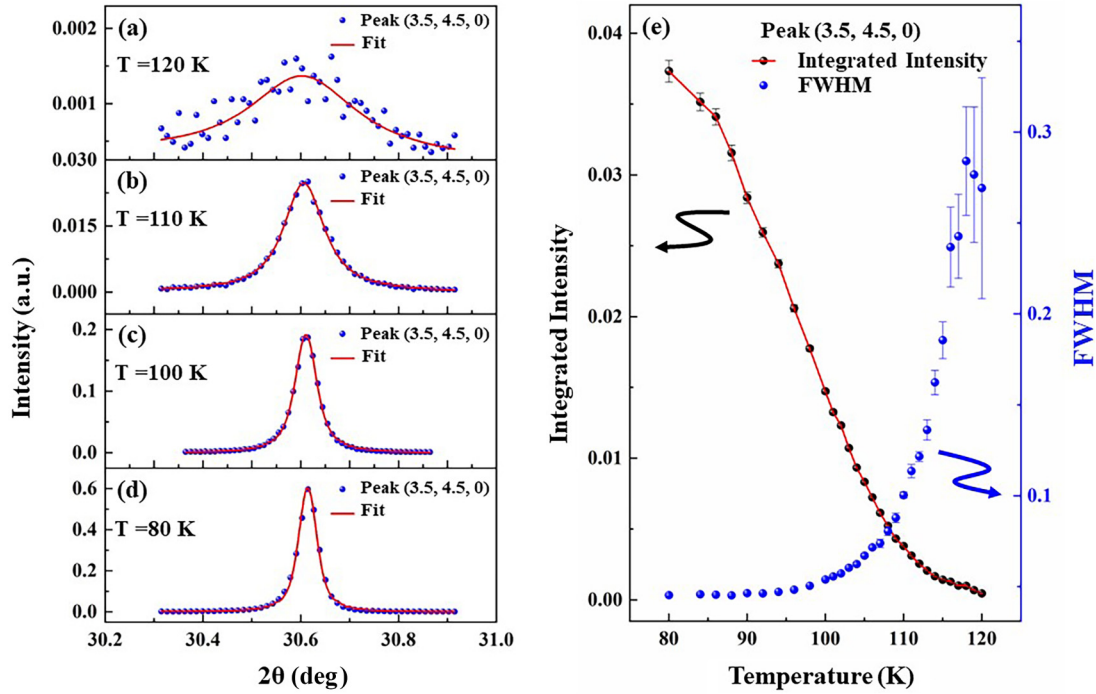


FIG. 3. (a)–(d) Evolution of (3.5,4.5,0) satellite XRS peak at various temperatures, fitted with the Voigt function. (e) Temperature dependence of the integrated intensity and FWHM of the (3.5,4.5,0) satellite peak.

system. Although the law describes paramagnetic materials, the fitting can provide a clear indication of the overall magnetic interaction in the system. Generally, a positive θ_{CW} value indicates FM ordering whereas a negative θ_{CW} value represents AFM ordering. In this case, θ_{CW} was -10.4 K, which is consistent with an earlier report on PCS [50]. Thus, the magnetic interaction in the system is identified as AFM. The AFM interaction may arise from the Co and/or Pr spins in the PCS. The magnetic moment was calculated from the Curie-Weiss fit of the inverse susceptibility data. The effective magnetic moment μ_{eff} is found to be $3.40\mu_B$, which is slightly less than the theoretical value of $3.58\mu_B$ for a free Pr^{3+} ion ($4f^2, J = 4$) [51]. The reduced μ_{eff} suggests the presence of hybridization between the Pr $4f$ electrons and conduction electrons or CT effects that partially screen the magnetic moment of the Pr ions. The first derivative of the ZFC susceptibility was also plotted against the temperature (see the inset of Fig. S4 in the SM) which also shows no transition in the temperature range (100–200 K).

To further identify potential CDW modulation, temperature-dependent XRS was conducted on single-crystal PCS. A series of new satellite features in PCS were observed when the temperature fell below 120 K. The behavior of one of these features (3.5,4.5,0) at various temperatures (80–120 K) was studied in detail. The red line in Figs. 3(a)–3(d) represents the XRS feature of PCS from (3.5,4.5,0) present at 80, 100, 110, and 120 K, fitted by the Voigt function. Basically, the satellite features in the XRS pattern arise from interference between the waves that were scattered by the modulated structure whose periodicity is shorter than the period of the main scattering feature [52]. The similar satellite features [(4.5,0.5,0) and (4.5,1.5,0)] in the XRD patterns of PCS at low temperatures [right inset in

Fig. 1(b)] and, consistently, the satellite features in the XRS [Figs. 3(a)–3(d)] are associated with a common direction, i.e., (0.5,0.5,0). Thus, the presence of these satellite features indicates modulation or distortion of atomic sites and the generation of a new q vector in the (0.5,0.5,0) direction below the transition temperature [52]. Evidently, the satellite feature in the XRS appeared at/below 120 K and intensified and/or became sharper as the temperature declined. Figure 3(e) presents the integrated intensities (FWHM) of the feature (3.5,4.5,0) of PCS in the temperature range 80–120 K, clearly revealing a monotonous decrease (increase) in the intensity (FWHM) as the temperature increased from 80 to 120 K. This effect can be understood as a result of the increase in the Debye-Waller factor (DWF) owing to structural instability/distortion in PCS at high temperatures [52]. Above 120 K, the integrated intensity is almost negligible and the FWHM is immeasurable, indicating that the modulated structure is stable only at or below this temperature. Importantly, the XRS [Fig. 3(e)] and low-temperature XRD [Fig. 1(b)] results suggest that the system probably undergoes a second-order phase transition at T^* , as no significant change in the cell volume of PCS is observed (Table II). Moreover, the modulated structure develops into a long-range order phase but exhibits deviating behavior of atomic vibration in the structure above $T = 120$ K; only a little distortion in the lattice is needed to generate such modulation, giving rise to a new q vector along (0.5,0.5,0). As stated above, Otomo *et al.* explained the superlattice formation in single-crystal $Ce_3Co_4Sn_{13}$ with reference to satellite features in XRD patterns that revealed similar cell-doubling transition [13]. In recent works, strong electron-phonon coupling and a second-order phase transition were observed in $Sr_3Ir_4Sn_{13}$ and $Sr_3Rh_4Sn_{13}$; in these studies, the trends in the intensity

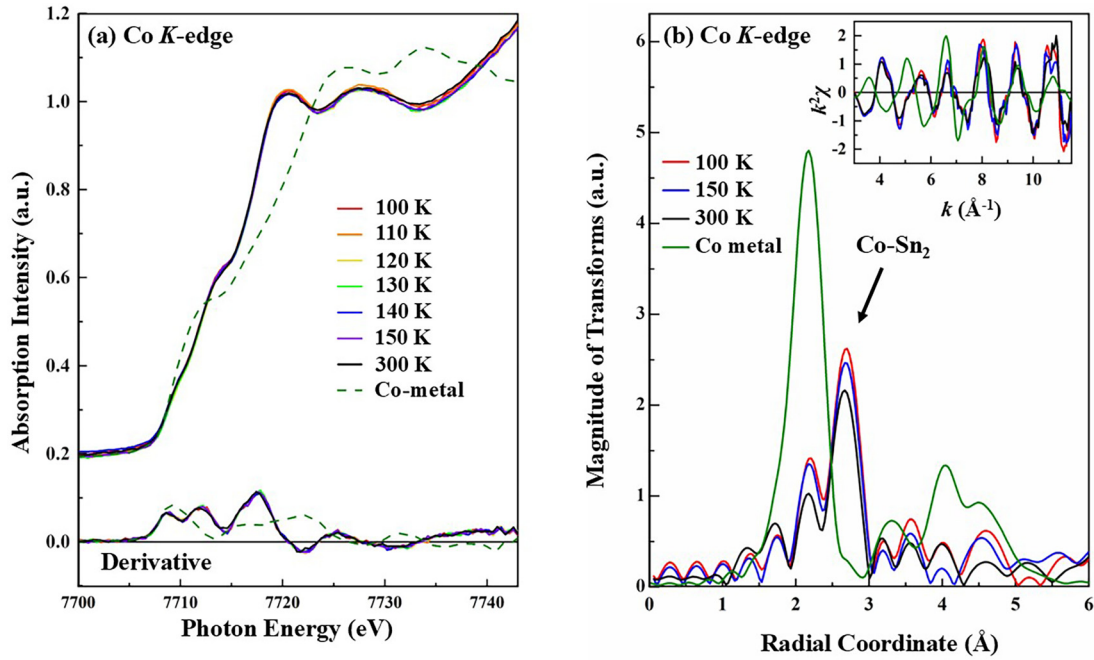


FIG. 4. (a) Temperature dependence of the normalized Co K -edge XANES spectra of single-crystal PCS along with the standard Co metal. Bottom panel shows the first derivative of each spectrum. (b) FT of EXAFS spectra at the Co K edge of single-crystal PCS at 100, 150, and 300 K.

and the FWHM of the (3.5,4.5,0) satellite feature in XRS were similar to observe. Many have controversially argued that such a superlattice formation is proof of CDW formation in the structure [7–9,11,12,14,15]. However, in the present case the formation of a superlattice does not involve a transition from a simple cubic phase ($Pm\bar{3}n$ space group) to a body-centered cubic phase ($I\bar{4}3d$ space group), rather the unit cell of the crystal structure is multiplied by the formation of a modulated structure.

B. Co and Sn K -edge absorption spectroscopy

Figure 4(a) shows the normalized Co K -edge XANES spectra of PCS at various temperatures from 300 to 100 K, and of Co metal at room temperature. The primary feature in the Co K -edge XANES spectra corresponds to the Co $1s \rightarrow 4p$ transition that is based on the dipole-selection transition rule, and the intensity of this feature is proportional to the density of the unoccupied Co $4p$ states [53]. The lower panel of Fig. 4(a) presents the first derivatives of the XANES spectra, from which the threshold features are used to determine the valence state of Co in PCS. The position of the leading first derivatives of the temperature-dependent XANES spectra at the Co K -edge XANES of PCS matches that of the reference Co metal, clearly indicating that the valence state of the Co atoms in PCS is close to zero, which is likely that of Co metal [46]. Only some distortion in the general line shape of the XANES spectra is observed, indicating the effect of different atomic environments at Co sites in PCS and thus the presence of Pr and Sn in the PCS and their interaction with Co atoms is different from that of Co metal. Moreover, the positions of the leading first derivatives remain constant throughout the

temperature range of 300 to 100 K. Accordingly, the valence state of Co in PCS not only is likely to be that of metallic Co but also does not change from high temperature (300 K) to low temperature (100 K). The difference between the atomic environments around Co atoms in PCS and Co metal is evident in the Fourier transform (FT) of the Co K -edge EXAFS of PCS at $T = 300, 150$, and 100 K and of Co metal (at room temperature), which are presented in Fig. 4(b). The inset shows the corresponding EXAFS ($k^2\chi$) oscillations. Quantitative details of the short-range local environment of Co sites in PCS, such as the coordination number, bond length, and DWF, are derived from an analysis of the Co K -edge EXAFS, which was performed using the Artemis program. Artemis combines the multiple-scattering EXAFS computer program FEFF with the nonlinear least-squares-fitting computer program FEFFIT [54]. Careful examination of the atomic structure [inset in Fig. 1(a)] reveals that the nearest neighbor (NN) of EXAFS scattering from Co sites primarily consists of Sn₂ atoms in PCS. Therefore, the main FT feature (indicated by an arrow) in the EXAFS spectra of PCS corresponds to the first coordination shell of Sn to a Co atom so, Sn₂ can be extracted. The NN Co-Sn₂ bond distance is ~ 2.6 Å, which is consistent with the bond length that is determined from the Rietveld refinement of the XRD data (Table I). Notably, the NN bond length around Co sites does not significantly change with temperatures from 300 to 100 K [Fig. 4(b)]. However, the intensity of the FT feature of Co-Sn₂ increases as the temperature decreases, owing to a decrease in the DWF at low temperatures [52,55]. This observation is consistent with the XRS results in Fig. 3(e), which reveal a monotonous increase in integrated intensity and a decrease in the FWHM of the (3.5,4.5,0) satellite feature of PCS as the temperature decreases from 120 to 80 K.

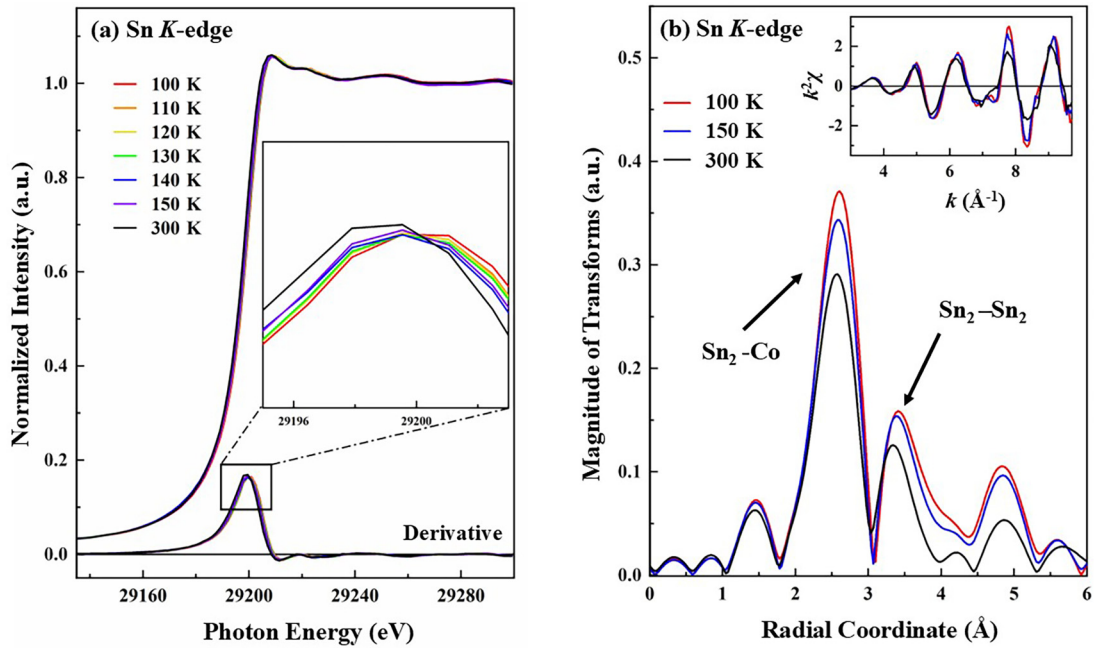


FIG. 5. (a) Temperature dependence of the normalized Sn K -edge XANES spectra of single-crystal PCS. Inset shows the first derivative of spectra obtained at 100, 150, and 300 K. (b) FT of EXAFS spectra at the Sn K edge of single-crystal PCS at 100, 150, and 300 K.

Figure 5(a) presents Sn K -edge XANES spectra of PCS at temperatures from 300 to 100 K. The absorption feature of Sn K -edge XANES corresponds to the Sn $1s \rightarrow 5p$ dipole-selected transition and the intensity of this feature is proportional to the number of unoccupied Sn $5p$ states in PCS. Investigation of the main feature in the absorption spectra and its first derivatives (bottom panel) clearly reveal that the latter shifts progressively to a higher energy (~ 1.2 eV) as the temperature decreases from 300 to 100 K. Although the shift is very small relative to the incident photon threshold energy ($\sim 29\,200$ eV) and the resolution of the beamline at that energy range (~ 1 eV), it is steady, as observed in the magnified plot in the inset of Fig. 5(a). This shift to higher energies implies a slight increase in the valence state of the absorbing Sn in PCS under consideration as the temperature decreases, as a result of the loss of more electrons from Sn $5p$ orbitals [56,57].

Figure 5(b) displays the FT of the EXAFS spectra at the Sn K edge of PCS that were obtained at temperatures 300, 150, and 100 K. Two major features are observed: they correspond to the NN and next-nearest-neighbor (NNN) coordination at ~ 2.6 and $3.3\text{--}3.4$ Å. As stated previously, the ~ 2.6 Å is the NN $\text{Sn}_2\text{-Co}$ bond length, consistent with the Co K -edge EXAFS result [Fig. 4(b)]. The $3.3\text{--}3.4$ Å represents the bond lengths host Sn—specifically $\text{Sn}_2\text{-Sn}_2/\text{Pr}$ and $\text{Sn}_2\text{-Sn}_1$, which can be referred to from Table I. The asymmetric nature of the Sn K -edge FT feature around $3.3\text{--}3.4$ Å establishes that the feature arises from multiple/different scattering effects, rather than from only single/same backscattering atoms that surround absorbing Sn atoms [57]. Close examination of the atomic structure, which is the largest contributor to the NNN FT feature in Fig. 5(b), indicates the most of $\text{Sn}_2\text{-Sn}_2/\text{Sn}_1$ bond lengths in the feature of PCS [inset in Fig. 1(a)]. Interestingly, the NN FT feature at ~ 2.6 Å exhibits no observable change as the temperature is lowered to 100/150 K

from 300 K. In contrast, the NNN FT feature exhibits an increase in bond lengths, predominantly $\text{Sn}_2\text{-Sn}_2/\text{Sn}_1$ bonds as the temperature decreases, indicating localized modulation of the $\text{Sn}_2\text{-Sn}_2/\text{Sn}_1$ bond lengths around Sn sites in PCS. Interestingly, the peak intensity of the FT of EXAFS shown in Fig. 5(b) is seen to increase below 150 K. The enhanced peak intensities in the Fourier-transformed EXAFS data correspond to reduced thermal vibrations and improved structural ordering at lower temperatures.

C. Co $L_{3,2}$ -edge and Pr $M_{5,4}$ -edge absorption spectroscopy

Figure 6(a) displays XANES spectra of PCS at the Co $L_{3,2}$ edge at 300, 150, and 100 K. The XANES data were normalized following the standard procedure of dividing the raw absorption data by the incident photon flux, then making the pre-edge to zero and the post-edge to the value 1. This normalization minimizes instrumental variations and allows for accurate comparisons of temperature-dependent spectral features. Since the Co $L_{3,2}$ absorption features are primarily generated by the electric dipole-selected transition Co $2p \rightarrow 3d$, they are highly sensitive to the oxidation state, spin state, and bond covalency of Co [55,56,58]. The spectra in Fig. 6(a) include two features at ~ 779 eV (L_3 edge) and ~ 794 eV (L_2 edge) that are separated by spin-orbit splitting and are related to the Co $2p\text{-}3d$ electrostatic interaction and density of Co $3d$ unoccupied states in PCS. Theoretical calculations (discussed below) reveal that some Co $3d$ states lie near/at the E_F of PCS. Any change in these Co $L_{3,2}$ -edge XANES spectra with temperature can alter the density of states (DOS) profile of the material near/at E_F . Notably, the shoulder that is observed at high photon energy at the Co L_3 edge yields a broad feature (shaded in blue) in the absorption region from approximately 780 to 784 eV. This feature has also been observed in the Ni L_3 -edge XANES of NiO and is typically identified as a

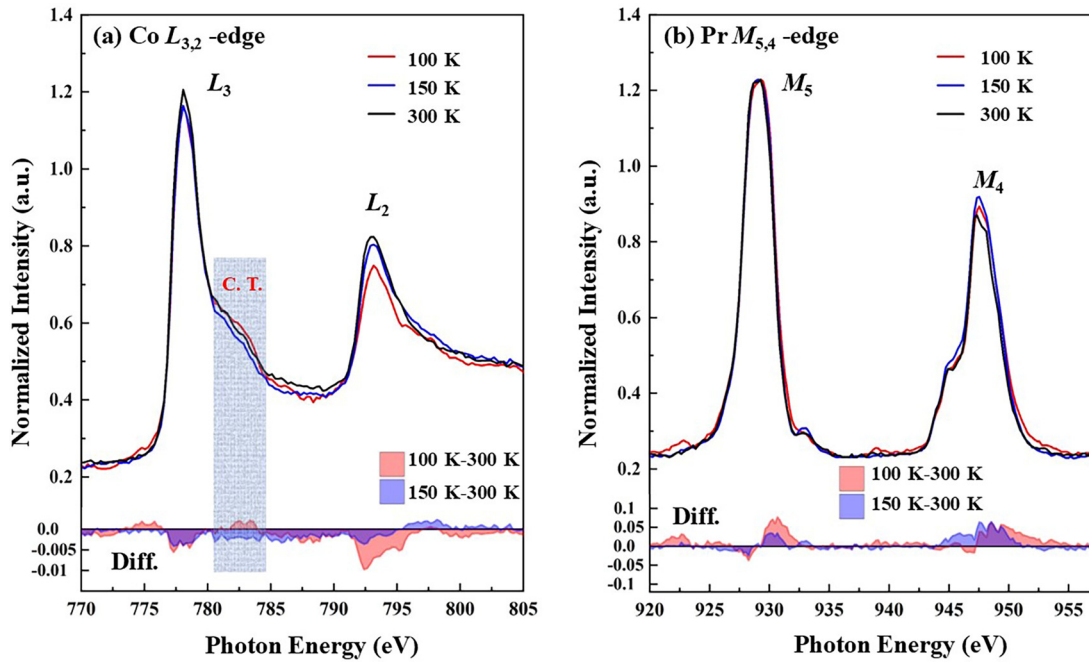


FIG. 6. (a) Temperature dependence of the normalized Co $L_{3,2}$ -edge XANES spectra of single-crystal PCS at 100, 150, and 300 K. (b) Temperature dependence of the normalized Pr $M_{5,4}$ -edge XANES spectra. Bottom panels in both figures show differences between the low-temperature and room-temperature spectra.

CT feature of a ligand state [59]. In the ground state, NiO exhibits hybridization between $3d^8$ and $3d^9\bar{L}$ owing to CT from ligand-oxygen to Ni ions, where \bar{L} denotes a hole in the O $2p$ band. CT was also observed in the RIXS spectra of PCS that were recorded at a certain photon energy around the L_3 edge of Co (see Fig. S5 in the SM). It was observed only when the incident photon energy exceeded 780 eV. The lower panel of Fig. 6(a) shows a difference between the absorption feature of PCS at the two lower temperatures (100 and 150 K) and that recorded at room temperature (300 K). Overall, the difference is mostly negative at the absorption feature at the $L_{3,2}$ edge in both lower-temperature cases, and it is clearly visible when the results at 100/150 and 300 K are compared. This finding suggests a reduction in the number of Co $3d$ unoccupied states above E_F , revealing an increase in CT phenomena in PCS as the temperature is lowered from 300 to 100/150 K. The temperature-dependent change in the peak intensities is more prominent in the L_2 edge where the 100 K data shows significant reduction in the peak intensity. This indicates the fact that the CT from Co enhances at low temperatures and the sudden increase below 150 K is possibly responsible for the transition observed in the C_p measurement and the structural modulation observed from the XRD and XRS measurements.

Figure 6(b) presents Pr $M_{5,4}$ -edge XANES spectra of PCS that were acquired at 300, 150, and 100 K. The two main features in the spectra are attributed primarily to electronic transitions from Pr $3d_{5/2}$ and $3d_{3/2}$ states to $4f$ states [60]. A separation between the two features at the M_5 and M_4 edge is attributed to the Pr spin-orbit interaction. In general, the $4f$ electrons are highly localized and interact weakly with their neighbors [7,9,11,56,58]. The lower panel of Fig. 6(b) also shows the difference between the spectra that were recorded

at temperatures of 100 and 150 K and that recorded at 300 K. The figure reveals that the number of unoccupied states above E_F increases as the temperature decreases, indicating an increase in the density of Pr $4f$ unoccupied states in PCS as the temperature decreases particularly to 100 K. From the XANES data at the Pr $M_{5,4}$ edge and the Co $L_{3,2}$ edge, CT occurred in PCS, but the key difference between the CT observed at the Pr $M_{5,4}$ and the Co $L_{3,2}$ edge is that the former was associated with an increase in the intensity of Pr $4f$ unoccupied states (at the Pr $M_{5,4}$ edge) as the temperature decreased from 300 to 150 K and further to 100 K whereas the latter was associated with a decrease in the intensity of the Co $3d$ unoccupied states (at the Co $L_{3,2}$ edge) in similar temperature variations. The opposite changes in intensity for the two elements Pr and Co in PCS signifies the different directions of CT in the two elements. In fact, the decrease in intensity that is observed in the case of Co demonstrates that electrons occupy more of the $3d$ states of Co, whereas the increase in intensity in the case of Pr reveals that electrons leave the $4f$ states of Pr. Therefore, these XANES spectra in Figs. 6(a) and 6(b) provide a clear picture of $f-d$ hybridization, in which the Pr $4f$ states donate electrons to the Co $3d$ states. However, $f-d$ hybridization is influenced by several factors, such as electronegativity, crystal-field symmetry, oxidation state, and the overlap of orbitals, among others [60]. The higher electronegativity of Co (1.88) than that of Pr (1.13) is consistent with the actual direction of the CT process [56]. However, the bond distances of Co-Sn₂ (~ 2.57 Å) and Co-Pr (~ 3.38 Å) suggest that the probability of Co $3d$ -Sn₂ $5p$ hybridization exceeds that of Co $3d$ -Pr $4f$ hybridization [56,57]. The shift of the XANES main feature at the Sn K edge [Fig. 5(a)] thus can also be explained by increased valence around the Sn due to Co, which is the NN to Sn₂ sites and loses more

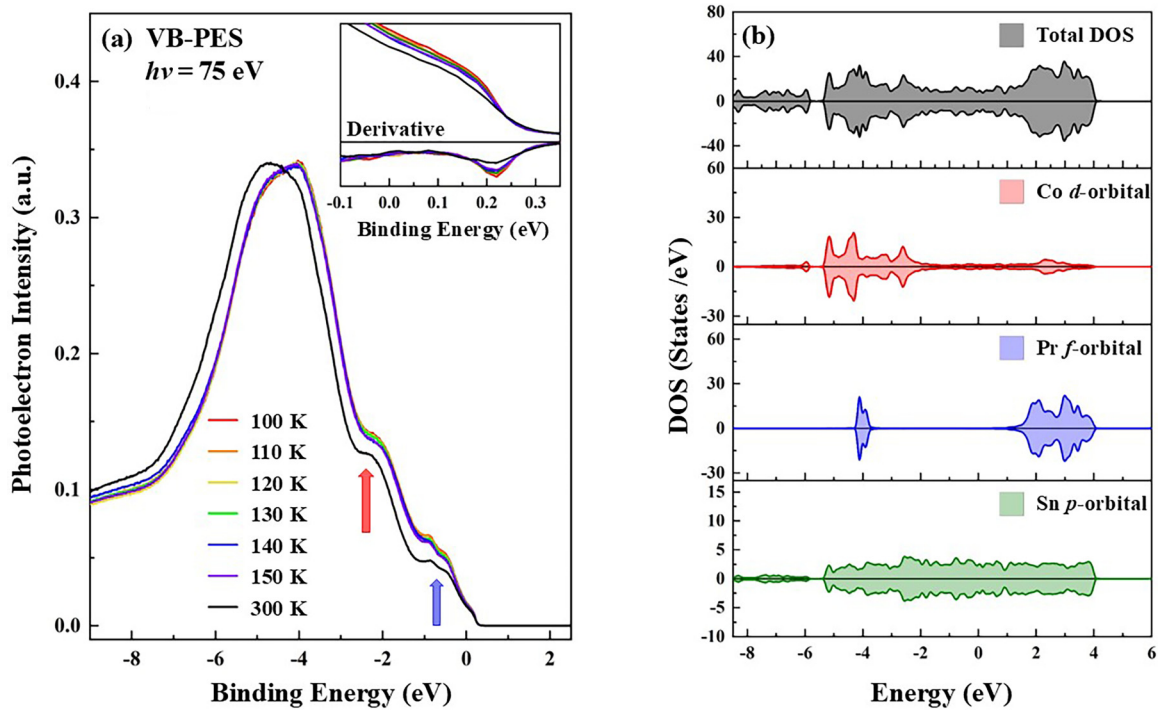


FIG. 7. (a) VB-PES of single-crystal PCS at various temperatures. Top inset magnifies the area near/at E_F . Bottom inset shows the first derivative of VB-PES spectra. (b) Spin-dependent DOSs at room temperature calculated using VASP via GGA.

electrons through Co 3d-Pr 4f hybridization as the temperature decreased [56,57].

D. Theoretical study and VB-PES

To study the DOS near/at E_F in PCS and to determine whether a gap and a clear kink, which was observed in $C_p(T)$ measurements around T^* , VB-PES spectra of PCS below and above 138 K were obtained. Spin-resolved DFT calculations were also performed to support the experimental DOS profile. The temperature-dependent VB-PES spectra of PCS were obtained at an excitation photon energy of $h\nu = 75.0$ eV with a resolution of ~ 10 meV, which is sufficient to detect any changes even ~ 10 –50 meV in the DOS. Figure 7(a) displays temperature-dependent VB-PES spectra and the inset magnifies the region at/near E_F and shows the derivatives of the spectra. Just above the $E_F \sim 0.2$ eV, the intensity starts to increase and the significant spectral weight near/at E_F suggests the metallic nature of PCS, which was also evidenced by the temperature-dependent resistivity study (upper inset in Fig. 2). Three broad features are observed in the VB spectra; two of them are at energies of around -0.6 and -2.2 eV (indicated by blue and red arrows) and the strongest is a wide feature (approximately -3 to -7 eV) that is centered at -4.7 eV. A comparison with the theoretical calculations in Fig. 7(b) allows the spectral weight at/near E_F to be attributed to Sn 5p, Co 3d, and Pr 4f orbitals. As can be determined from the DFT calculation, the feature at -2.2 eV is associated with the Co 3d orbital. The strongest feature that is centered at -4.7 eV is due primarily to prominent Co 3d and Pr 4f orbitals on a DOS background of an Sn 5p orbital, as determined from the DFT figure. The XANES spectra at the Co $L_{3,2}$ edge and the Pr $M_{5,4}$ edge provide evidence of

hybridization between Co 3d and Pr 4f orbitals. The DFT calculation shows an overlapping of Co 3d orbitals with the Pr 4f orbital near -4 eV in the valence band, which is responsible for the widest feature of the VB-PES. Thus, the DFT calculation and the VB-PES spectra corroborate the XANES results and confirm the hybridization of Co 3d and Pr 4f orbitals and, consequently, the CT process between them, as observed in Figs. 6(a) and 6(b) and in the RIXS data in Fig. S5 in the SM. Interestingly, the VB-PES spectra that are measured at 150 K and below are seen to be slightly different from that measured at 300 K, which reflects a modification in the electronic states. Upon closer examination, we note that the VB-PES spectra for all temperatures (80–300 K) show a consistent shift of ~ 0.3 eV above the E_F . This observation suggests that the feature is not solely due to thermal broadening but may instead reflect a systematic calibration offset or an intrinsic property of the material. The observed shift could reflect intrinsic electronic effects, such as unoccupied states slightly above the E_F due to the material's unique electronic structure. The inset in Fig. 7(a) presents the derivatives of the VB-PES spectra, whose minimum at an energy of -0.2 eV is the E_{VBM} . Importantly, the position of minimum does not change with temperature from 100 to 300 K, indicating that the E_{VBM} of PCS does not change with temperature. The Co $L_{3,2}$ -edge and Pr $M_{5,4}$ -edge XANES spectra obtained at various temperatures show that the DOS near/at E_F of the system that comprises Co 3d and Pr 4f orbitals, based on DFT calculations, undergoes no significant change. These results confirm the lack of change of position in the conduction-band minimum (E_{CBM}) for PCS. Therefore, the DOS profile of the PCS system that is obtained from the DFT calculations and the experimental XANES and VB-PES demonstrate that the band gap (within experimental

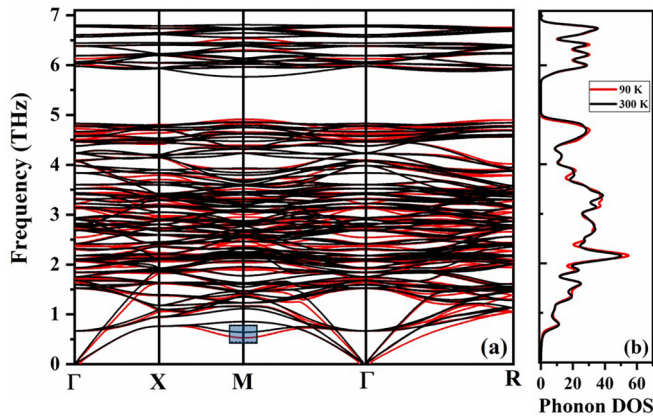


FIG. 8. Phonon spectrum (left panel) and phonon DOS (right panel) of PCS calculated using experimental lattice constants at 300 and 90 K, respectively. A significant soft mode at point M is indicated in the blue region.

uncertainties) does not change with temperature (300–100 K). The energy level of the Co $3d$ states, which were studied in detail via RIXS (Fig. S5 in the SM), was found to be static throughout the temperature range (80–300 K) with various incident photon energies. Generally, in $RE_3TM_4Sn_{13}$ structures, the $3d$ states of the TM and the $5p$ states of Sn constitute the DOS at/below E_F [12]. The fact that the energy level of $3d$ states of Co at/below E_F in PCS remains almost constant below and above the observed temperature of T^* , implies that the band gap of PCS does not change observably from room temperature (300 K) to low temperature (80 K). This result confirms that the PCS system does not undergo a CDW-like transition near T^* as no band-gap opening is detected and such an opening is a primary characteristic of CDW modulation.

To study the possible temperature-induced structural phase transition of PCS, phonon band-structure calculations were performed. Figure 8(a) presents the phonon spectra at 300 and 90 K that were calculated using lattice parameters that were experimentally evaluated from the XRD data at those temperatures [Fig. 1(b)]. The notations Γ , R , X , and M in the

figure are points of high symmetry in the Brillouin zone of the crystal. From the calculated phonon spectrum and DOS at both the temperatures, shown in Fig. 8(b), cubic PCS with the experimental lattice constant was stable as no imaginary frequency of the phonons was found. However, a softening feature of the lowest-frequency mode with a frequency of 0.761 THz at 90 K, indicated by the blue shaded region at the point M (0.5,0.5,0), implies a precursor to thermal instability of the structure as a result of the effects of temperature on the lattice constants. While similar ternary stannides $Sr_3Ir_4Sn_{13}$ and $Ca_3Ir_4Sn_{13}$ clearly exhibit structural instability, revealed by an imaginary frequency, $La_3Co_4Sn_{13}$ shows only softening of the phonon mode at the point M [38], as in the present case in which it is also a precursor to instability. Since the point M represents the (0.5,0.5,0) direction, the softening of the phonon modes clearly supports the experimental findings herein, based on XRD and XRS, of structural modulation through the formation of a new q vector in the same direction (0.5,0.5,0). Interestingly, the structure is drawn in a manner guided by the corresponding eigenvector of this soft mode at the point, as in Figs. 9(a) and 9(b), each Sn_1 -12 Sn_2 icosahedron is surrounded by an 8Co-6 Sn_2 triangular-prism cage and experiences a small distortion to form a $2 \times 2 \times 1$ supercell. In this supercell the unit cell of the crystal structure multiplies as a result of the transformation. Figure 9(c) compares the calculated XRD pattern of the phonon-guided supercell structure (shown in red) and the calculated XRD pattern of the structure at room temperature (shown in black) within the small-angle range of $2\theta = 42.5^\circ$ – 44.5° with the experimental XRD patterns at 300 and 90 K (shown in green and blue, respectively). Notably, the calculated XRD pattern of the supercell structure in that range includes four distinct satellite peaks similar to the satellite features that are observed at 90 K. This observation is particularly intriguing because it is consistent with our experimental findings, as shown in the inset of Fig. 1(b), that such small features arise when the temperature is below 120 K and a clear feature is observed at 90 K. Unsurprisingly, indexing of the XRD data shows that these features arose from the formation of a new q vector

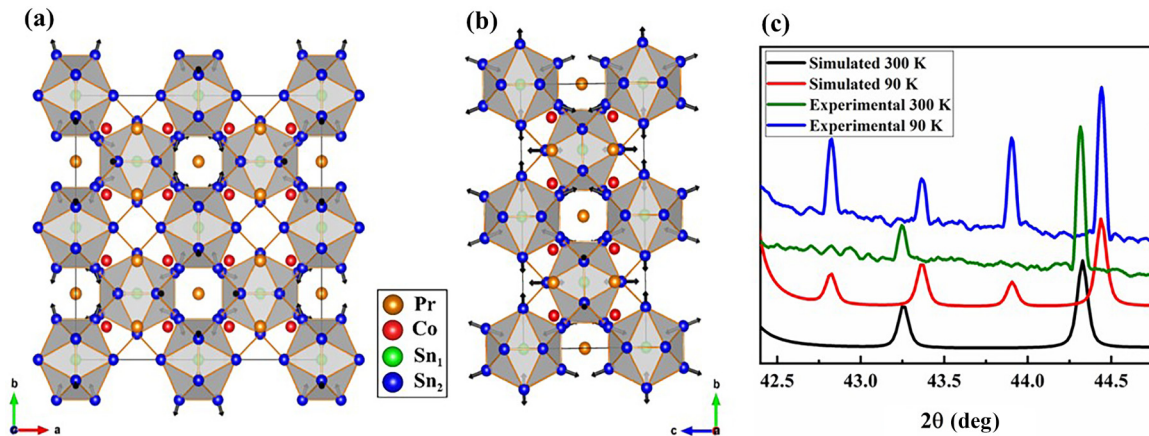


FIG. 9. Calculated eigenvector (black arrows) of the lowest-frequency mode at point M of a $2 \times 2 \times 1$ supercell on (a) the ab plane and (b) the bc plane. Sn_1 (green)-12 Sn_2 (blue) icosahedra represented by gray cages is surrounded by eight Co (red)-6 Sn_2 (blue) triangular prisms. (c) Calculated powder XRD pattern at 300 K (black curve) and a $2 \times 2 \times 1$ supercell structure (red curve) modulated by the eigenvector in (a) and (b) along with the normalized observed XRD patterns at 90 K (blue curve) and 300 K (green curve).

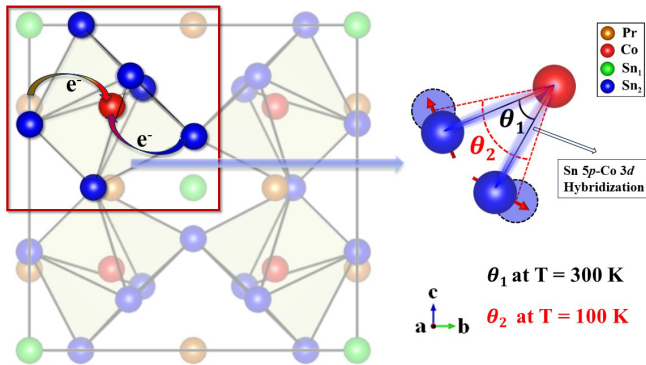


FIG. 10. Schematic representation of the $\text{Sn}_2\text{-Co-Sn}_2$ trigonal prism and the $\text{Sn}_2\text{-Co-Sn}_2$ bond elongation in the cubic-octahedral site before and after transition.

in the $(0.5,0.5,0)$ direction. Thus, these satellite features that are observed at low temperatures strongly indicate the formation of a supercell structure when the temperature drops below 120 K. This correlation between the calculated and experimental data clearly establishes the temperature-dependent structural changes that lead to the emergence of a supercell configuration.

IV. DISCUSSION

From the results of EXAFS at the Co K edge and XANES at the Sn K , Co $L_{3,2}$, and Pr $M_{5,4}$ edges, two important characteristics of PCS and its structure at various temperatures are identified. They are (i) modulation of the structure via $\text{Sn}_2\text{-Sn}_2$ bond elongation in the cubic-octahedral site mainly and (ii) an anomaly or change in unoccupied states at low temperatures due to CT, resulting in the hybridization of Co $3d$ -Sn $5p$ /Pr $4f$ and/or Pr $4f$ -Sn $5p$ states. These two processes, along with the structural modulation that is identified from XRS/XRD and XANES/EXAFS results, are enough to determine the origin of the observed clear kink in the $C_p(T)$ measurements. The bond angle of $\text{Sn}_2\text{-Co-Sn}_2$ can easily be derived from the bond lengths that are estimated from the radial coordinates of EXAFS because two Sn_2 atoms form a triangle with a Co atom in the cubic-octahedral site. Figure 10 schematically depicts this phenomenon with the two bond angles θ_1 and θ_2 at 300 and 100 K, respectively. Calculations of the bond angle reveal that as the temperature decreases from 300 to 100 K, the bond angle increases from $\theta_1 = 80.9 \pm 0.1^\circ$ to $\theta_2 = 81.5 \pm 0.1^\circ$. The modulation of the local atomic structure from the EXAFS spectra of PCS that are acquired at the Sn K edge reveals that the overall structure of the $\text{Sn}_2\text{-Co}$ trigonal prism in the cubic-octahedral site is slightly increased due to elongation of the $\text{Sn}_2\text{-Sn}_2$ bond [Fig. 5(b)] and thus an increase in the bond angle at low temperatures. This subtle distortion also affects each $\text{Sn}_1\text{-12Sn}_2$ icosahedron that is nestled within eight Co-6Sn_2 triangular-prism neighbors, leading to the formation of a supercell, as was determined from our phonon calculations. We believe that this distortion is a second-order phase transition in which structural modulation involves a diffusionless process [61]. The directions of the Sn_2 atom movement in Fig. 10 are consistent with the direction of the eigenvectors

of the atoms that are obtained from our phonon calculations [Figs. 9(a) and 9(b)]. This results in structural modulation or the generation of a new q vector in the $(0.5,0.5,0)$ direction, as observed from the XRD and XRS studies [13,62,63]. Comparing lattice parameters that are obtained from low-temperature XRD results (Table II) and the bond lengths that are determined from the low-temperature EXAFS results suggests a contradiction in that the lattice parameters decrease whereas bond length ($\text{Sn}_2\text{-Sn}_2$) increases as the temperature decreases. The phenomenon of increasing bond length but decreasing lattice parameter with decreasing temperature is an effect of negative thermal expansion (NTE) [64,65]. Depending on the electron-phonon interactions, some bonds in the material can be “softened” and elongate, while others remain relatively unchanged. The elongated bonds contribute to thermal expansion, but other factors such as changes in electronic energy, Coulomb interaction among the constituent atoms, and the overlap of orbitals, can cause contraction of the lattice. A study of phonon behavior (Fig. 8) has revealed that one phonon mode at point M $(0.5,0.5,0)$ that corresponds to the CoSn_6 octahedron (Fig. 9) is softened at low temperatures, causing the structural modulation of the system. Indeed, the partial phonon density of states calculations (as shown in Fig. S6 in the SM) reveal that the softening of the lowest-frequency phonon mode at 0.761 THz at 90 K is predominantly associated with the displacement of Sn atoms. This finding supports the model of structural modulation driven by lattice instabilities at low temperatures. Interestingly, the formation of CDW can induce NTE as strong electron-phonon couplings are one of its key features, which can cause the softening of phonon modes. NTE has been observed in many systems that exhibit CDW, such as $\eta\text{-Mo}_4\text{O}_{11}$ and $1T\text{-NbSe}_2$ [64,65].

The results that are observed from XANES spectra recorded at the Co $L_{3,2}$ and Pr $M_{5,4}$ edges can be easily related to the shifting of the XANES feature recorded at the Sn K edge to higher energy at low temperatures [inset of Fig. 5(a)]. The shift is possible because the Sn atoms most likely donate electrons to minimize their energy by having more unoccupied/empty outermost shells (increasing their valence state). Co atoms exhibit a reduction in intensity of the Co $L_{3,2}$ -edge XANES feature at low temperatures, indicating a decrease in the density of the unoccupied Co $3d$ states, showing acceptance of electrons into the $3d$ orbitals of Co at low temperatures. The Pr $M_{5,4}$ -edge XANES spectra show an increase in the intensity of the XANES feature as the temperature decreases, indicating an increase in the density of the unoccupied states of Pr $4f$ states due to the electrons leaving the $4f$ orbitals of Pr. The DFT calculations indicate significant overlapping of the Sn $5p$, Co $3d$, and Pr $4f$ states in PCS near/at E_F , which favors their hybridization. Thus, these measurements show that Co atoms play a central role in the low-temperature physics of PCS as Co $3d$ states bond with Sn $5p$ as well as Pr $4f$ by CT. The reduced μ_{eff} value of PCS (than that of free Pr^{3+} ions) evaluated from the Curie-Weiss fit of the inverse susceptibility data (see Fig. S3 in the SM) also suggests the presence of hybridization between the Pr $4f$ electrons and conduction electrons or CT effects that partially screen the magnetic moment of the Pr ions. At low temperatures, as the Sn atoms donate a few electrons by

CT to Co as a result of Co 3*d*-Sn 5*p* hybridization, the atom relaxes from its original position resulting in an increase in the Sn₂-Sn₂ bond distance in the cubic-octahedral site. Similar CT from each Sn₂ (−0.004*e*) to Co (+0.008*e*) as a result of decreasing temperature was also determined from DFT results by a Bader charge analysis [66]. The presence of DOS slightly above the E_F (∼0.3 eV) also suggests hybridization enhanced redistribution of the electronics states. The electron density in the Co(Sn)₆ trigonal prism increases as the temperature decreases when Co 3*d* and Sn 5*p* interact and hybridize with Pr 4*f* states; this process may also be the cause of Sn₂-Sn₂ bond elongation. Whether the CT process is closely related to the structural modulation or whether one triggers the other is difficult to determine. However, our observations suggest that in the present case, they are related and structural modulation through the Sn₂-Sn₂ bond elongation is caused by the hybridization and CT process, resulting in a clear kink in the macroscopic C_p of the system. In fact, our VB-PES spectra [Fig. 7(a)] indicate that there is a change of electronic states of the materials even at 150 K, which can be attributed to the gradual onset of hybridization between the Co 3*d*, Sn 5*p*, and Pr 4*f* orbitals. This change appears to precede the structural instability observed at lower temperatures. While the electronic state changes at 150 K do not correspond directly to a C_p anomaly, they signify a precursor to the low-temperature structural transition. Moreover, the structural modulation by the generation of a new \mathbf{q} vector must have an effect on the phonon energies of the system, as was determined from our theoretical calculations that revealed one of the phonon modes that corresponds to CoSn₆ octahedra at point M (0.5,0.5,0) is softened at low temperatures. The softening of these phonon modes, which reflect the Co(Sn)₆ octahedral vibrations, suggests that this structural modulation alters the lattice's vibrational dynamics, contributing to the C_p anomaly. Such phonon softening causes changes in the DWF, directly impacting the C_p through modifications in phonon density and energy distribution [52,63]. Such phonon-driven transitions have been similarly observed in related stannide systems like La₃Co₄Sn₁₃ and Sr₃Rh₄Sn₁₃, where local lattice instabilities contribute to C_p anomalies associated with structural phase transitions [14,38]. This correlation implies that although PCS does not exhibit CDW behavior, the observed local lattice distortion impacts phonon behavior, leading to the C_p anomaly at 138 K. The C_p anomaly observed at 138 K corresponds to a secondary phase transition, associated with local lattice distortions and structural modulation, as indicated by XRD and phonon calculations. This anomaly reflects the emergence of a temperature-dependent coupling between electronic and structural degrees of freedom, driven by enhanced hybridization. Although the temperatures for the C_p anomaly and electronic changes differ, they are interconnected, with electronic modifications at 150 K setting the stage for structural changes at 138 K. As shown in the XRD patterns [inset of Fig. 1(b)], superlattice reflections appear distinctly below 120 K, signifying the development of long-range structural order. This progression aligns with the multistage transition in PCS: the onset of electronic changes at 150 K, lattice instability at 138 K, and superlattice formation below 120 K. These stages reflect a sequential transition process, rather than a single abrupt change. Such transition process observed in

several other materials, often arises from complex interactions between structural instabilities and electronic degrees of freedom [67–69]. In 1*T*-TiSe₂, the structural transition occurs at a higher temperatures than the electronic transition to a CDW state [67], which is attributed to lattice distortions facilitating subsequent electronic ordering. In compounds like PrOs₄Sb₁₂, structural anomalies precede the onset of superconductivity [68,69] highlighting strong coupling between lattice and electronic states. Therefore, this study demonstrates that the PCS system undergoes a transition that is related to CT, causing structural instability through Sn₂-Sn₂ bond elongation mainly in the cubic-octahedral site. This bond elongation is also accompanied by phonon softening at point M (0.5,0.5,0) possibly as a result of electron-phonon coupling, which has been observed elsewhere [34,53]. Although these two effects have been argued by many to be the prerequisites for a CDW, a CDW may not form as no change in the DOS profile, which is to say no opening of the energy gap between E_{CBM} and E_{VBM} in DOS, has been observed [7,9,11,15]. RIXS measurements further provide evidence of the CT process and the fact that the band gap does not change with temperature since the RIXS features were static as the temperature changed (Fig. S5 in the SM). Resistivity measurements also do not show any transition around T^* , confirming that no CDW is formed. Our experimental results confirm that CDW is not formed in the PCS system at the temperatures of interest, whereas it is in several other $RE_3TM_4Sn_{13}$ materials [7,9,11,12,15]. Moreover, as in all other relevant reports concerning other materials, the trigonal prism of Co(Sn)₆ is crucial in the case of PCS. The conduction band in this work is primarily constituted of Co 3*d* and Sn 5*p* states with a contribution from Pr 4*f* states, as in earlier reports [14,15,25]. Although PCS undergoes structural modulation and the formation of a supercell such as Sr₃Ir₄Sn₁₃, Sr₃Rh₄Sn₁₃, or Ce₃Co₄Sn₁₃, unlike them, it does not exhibit CDW modulation [7,11,12,14]. In PCS, the structural distortions observed are insufficient to induce the periodic modulation in electron density necessary for CDW and the absence of CDW behavior in PCS can be attributed to distinct CT dynamics and structural characteristics, as revealed in our experimental observations. While the emergence of a new \mathbf{q} vector in the (0.5,0.5,0) direction and the associated structural modulation are often linked to CDW phenomena [7,11,12,14], these features alone are not definitive evidence of CDW formation. Our findings demonstrate that such structural changes can arise independently, possibly due to phonon softening or local lattice distortions, as supported by our XRD and phonon calculation results.

V. CONCLUSION

In conclusion, the local electronic, atomic, and crystal structures of high-quality single-crystalline PCS were studied to explore a potential CDW modulation of the structure and the strongly correlated Co *d*, Sn *p*, and Pr *f* states therein. A kink near ∼138 K was observed in measurements of the specific heat of the system. The measurement of resistivity and magnetization did not show any transition near that temperature, confirming the lack of involvement of spin ordering in the transition. XRD and XRS measurements revealed a

modulation of the structure and the generation of a new \mathbf{q} vector in the (0.5,0.5,0) direction was observed. XANES spectra that were recorded at the Sn K edge and the Co $L_{3,2}$ edge revealed an increase in the Sn valence state and a lowering of intensity of the Co $L_{3,2}$ -edge XANES with decreasing temperature as a result of CT due to Co $3d$ -Sn $5p$ hybridization. Sn K -edge EXAFS spectra recorded at various temperatures also revealed Sn₂-Sn₂ bond elongation, which is understood to cause structural modulation via a diffusionless process. An increase in the intensity of Pr $M_{5,4}$ -edge XANES was observed and explained by CT as a result of Co $3d$ -Pr $4f$ hybridization. The VB-PES spectra and DFT calculations provide evidence of Co $3d$ -Pr $4f$ hybridization. A VB-PES study of the sample at various temperatures revealed no change in its E_{VBM} . XANES spectra at the Co $L_{3,2}$ edge and the Pr $M_{5,4}$ edge reveal that E_{CBM} did not change, confirming a lack of change in the band gap of the PCS system with temperatures. This finding, together with the lack of any transition in the temperature-dependent resistivity of the sample, confirms the absence of CDW modulation in the structure despite a struc-

tural modulation and CT phenomena at low temperatures. The experimental results are well supported by our theoretical calculations, which revealed the formation of a supercell at low temperatures and softening of the phonon modes at point M . The calculated XRD patterns of the crystal structure and the supercell structure matches the XRD patterns that were obtained at high (300 K) and low temperatures (90 K). This study presents an effective method for detecting CDW formation in a structure.

ACKNOWLEDGMENTS

The authors (J.-W.C., H.-C.H., C.-S.L., and W.-F.P.) would like to thank the National Science and Technology Council (NSTC) of Taiwan for providing financial support for research under the Projects No. NSTC-113-2112-M-390-002, No. 113-2112-M-032-013, No. 112-2124-M-006-009, and No. 113-2112-M-032-001. The authors also acknowledge the computational resources and storage provided by National Center for High-Performance Computing (NCHC) in Taiwan.

-
- [1] P. Chen, W. Han, M. Zhao, J. Su, Z. Li, D. Li, L. Pi, X. Zhou, and T. Zhai, Recent advances in 2D rare earth materials, *Adv. Funct. Mater.* **31**, 2008790 (2021) and references therein.
 - [2] R. V. Skolozdra, in *Handbook on the Physics and Chemistry of Rare Earths*, edited by K. A. Gschneidner, and L. Eyring (Elsevier, Netherlands, 1997), Vol. 24, p. 399.
 - [3] G. R. Stewart, Heavy fermion systems, *Rev. Mod. Phys.* **56**, 755 (1984).
 - [4] M. A. Pires, L. M. Ferreira, J. G. S. Duque, R. R. Urbano, O. Agüero, I. Torriani, C. Rettori, E. M. Bittar, and P. G. Pagliuso, Crystal structure and physical properties of $\text{Gd}_3\text{Co}_4\text{Sn}_{13}$ intermetallic antiferromagnet, *J. Appl. Phys.* **99**, 08J311 (2006).
 - [5] U. Kohler, A. P. Pikul, N. Oeschler, T. Westerkamp, A. M. Strydom, and F. Steglich, Low-temperature study of the strongly correlated compound $\text{Ce}_3\text{Rh}_4\text{Sn}_{13}$, *J. Phys.: Condens. Matter* **19**, 386207 (2007).
 - [6] N. Kase, H. Hayamizu, and J. Akimitsu, Superconducting state in the ternary stannide superconductors $R_3T_4\text{Sn}_{13}$ ($R = \text{La, Sr; } T = \text{Rh, Ir}$) with a quasi-skutterudite structure, *Phys. Rev. B* **83**, 184509 (2011).
 - [7] C. S. Lue, H. F. Liu, S. L. Hsu, M. W. Chu, H. Y. Liao, and Y. K. Kuo, Observation of a possible charge-density-wave transition in cubic $\text{Ce}_3\text{Co}_4\text{Sn}_{13}$, *Phys. Rev. B* **85**, 205120 (2012).
 - [8] L. E. Klintberg, S. K. Goh, P. L. Alireza, P. J. Saines, D. A. Tompsett, P. W. Logg, J. Yang, B. Chen, K. Yoshimura, and F. M. Grosche, Pressure- and composition-induced structural quantum phase transition in the cubic superconductor $(\text{Sr, Ca})_3\text{Ir}_4\text{Sn}_{13}$, *Phys. Rev. Lett.* **109**, 237008 (2012).
 - [9] H. F. Liu, C. N. Kuo, C. S. Lue, K.-Z. Syu, and Y. K. Kuo, Partially gapped Fermi surfaces in $\text{La}_3\text{Co}_4\text{Sn}_{13}$ revealed by nuclear magnetic resonance, *Phys. Rev. B* **88**, 115113 (2013).
 - [10] A. Slebarski, J. Goraus, P. Witas, L. Kalinowski, and M. Fijałkowski, Study of d -electron correlations in skutterudite-related $\text{Ce}_3M_4\text{Sn}_{13}$ ($M = \text{Co, Ru, and Rh}$), *Phys. Rev. B* **91**, 035101 (2015).
 - [11] C. N. Kuo, C. W. Tseng, C. M. Wang, C. Y. Wang, Y. R. Chen, L. M. Wang, C. F. Lin, K. K. Wu, Y. K. Kuo, and C. S. Lue, Lattice distortion associated with Fermi-surface reconstruction in $\text{Sr}_3\text{Rh}_4\text{Sn}_{13}$, *Phys. Rev. B* **91**, 165141 (2015).
 - [12] C. S. Lue, C. N. Kuo, C. W. Tseng, K. K. Wu, Y.-H. Liang, C.-H. Du, and Y. K. Kuo, Comparative study of thermodynamic properties near the structural phase transitions in $\text{Sr}_3\text{Rh}_4\text{Sn}_{13}$ and $\text{Sr}_3\text{Ir}_4\text{Sn}_{13}$, *Phys. Rev. B* **93**, 245119 (2016).
 - [13] Y. Otomo, K. Iwasa, K. Suyama, K. Tomiyasu, H. Sagayama, R. Sagayama, H. Nakao, R. Kumai, and Y. Murakami, Chiral crystal-structure transformation of $R_3\text{Co}_4\text{Sn}_{13}$ ($R = \text{La and Ce}$), *Phys. Rev. B* **94**, 075109 (2016).
 - [14] H.-T. Wang, M. K. Srivastava, C.-C. Wu, S.-H. Hsieh, Y.-F. Wang, Y.-C. Shao, Y.-H. Liang, C.-H. Du, J.-W. Chiou, C.-M. Cheng *et al.*, Electronic and atomic structures of the $\text{Sr}_3\text{Ir}_4\text{Sn}_{13}$ single crystal: A possible charge density wave material, *Sci. Rep.* **7**, 40886 (2017).
 - [15] A. Singh, H. Y. Huang, Y. Y. Chin, Y. F. Liao, T. C. Huang, J. Okamoto, W. B. Wu, H. J. Lin, K. D. Tsuei, R. P. Wang *et al.*, Electronic structure investigation of a charge density wave coupled to a metal-to-metal transition in $\text{Ce}_3\text{Co}_4\text{Sn}_{13}$, *Phys. Rev. B* **98**, 235136 (2018).
 - [16] R. E. Peierls, *Quantum Theory of Solids* (Oxford University Press, New York, 1955).
 - [17] M. D. Johannes and I. I. Mazin, Fermi surface nesting and the origin of charge density waves in metals, *Phys. Rev. B* **77**, 165135 (2008).
 - [18] W. M. Lomer, Electronic structure of chromium group metals, *Proc. Phys. Soc.* **80**, 489 (1962).
 - [19] J. W. York, Jr., Gravitational degrees of freedom and the initial-value problem, *Phys. Rev. Lett.* **26**, 1656 (1971).
 - [20] D. Weaire, Existence of a gap in the electronic density of states of a tetrahedrally bonded solid of arbitrary structure, *Phys. Rev. Lett.* **26**, 1541 (1971).

- [21] S.-K. Chan and V. H. Heine, Spin density wave and soft phonon mode from nesting Fermi surfaces, *J. Phys. F: Met. Phys.* **3**, 795 (1973).
- [22] P. Monceau, N. P. Ong, A. M. Portis, A. Meerschaut, and J. Rouxel, Electric field breakdown of charge-density-wave—Induced anomalies in NbSe₃, *Phys. Rev. Lett.* **37**, 602 (1976).
- [23] T. Kiss, T. Yokoya, A. Chainani, S. Shin, T. Hanaguri, M. Nohara, and H. Takagi, Charge-order-maximized momentum-dependent superconductivity, *Nat. Phys.* **3**, 720 (2007).
- [24] M. F. Hundley, J. L. Sarrao, J. D. Thompson, R. Movshovich, M. Jaime, C. Petrovic, and Z. Fisk, Unusual Kondo behaviour in the indium-rich heavy-fermion antiferromagnet Ce₃Pt₄Sn₁₃, *Phys. Rev. B* **65**, 024401 (2001).
- [25] G. Zhong, X. Lei, and J. Mao, Chemical bonding, electronic, and magnetic properties of R₃Co₄Sn₁₃ intermetallics (R = La, Ce, Sm, Gd, and Tb): Density functional calculations, *Phys. Rev. B* **79**, 094424 (2009).
- [26] H. F. Liu, Single crystal synthesis and nuclear magnetic resonance study of R₃Co₄Sn₁₃ (R = La, Ce, Pr, Yb) intermetallics, 2016, Doctoral dissertation, National Cheng Kung University, Taiwan, NCKU depository <https://hdl.handle.net/11296/vkn2z7>
- [27] C.-L. Dong, J.-W. Chiou, H.-M. Tsai, H.-W. Fu, H.-J. Lin, C. T. Chen, and W.-F. Pong, Photon-in/photon-out soft x-ray spectroscopy at the TPS 45A Beamline, *Synchrotron Radiat. News* **30**, 24 (2017).
- [28] J. Rodríguez-Carvajal, Recent advances in magnetic structure determination by neutron powder diffraction, *Phys. B (Amsterdam, Neth.)* **192**, 55 (1993).
- [29] G. Kresse and J. Furthmüller, Efficient iterative schemes for *ab initio* total-energy calculations using a plane-wave basis set, *Phys. Rev. B* **54**, 11169 (1996).
- [30] G. Kresse and D. Joubert, From ultrasoft pseudopotentials to the projector augmented-wave method, *Phys. Rev. B* **59**, 1758 (1999).
- [31] J. P. Perdew, K. Burke, and M. Ernzerhof, Generalized gradient approximation made simple, *Phys. Rev. Lett.* **77**, 3865 (1996).
- [32] S. L. Dudarev, G. A. Botton, S. Y. Savrasov, C. J. Humphreys, and A. P. Sutton, Electron-energy-loss spectra and the structural stability of nickel oxide: An LSDA+U study, *Phys. Rev. B* **57**, 1505 (1998).
- [33] J. Chen, X. Wu, and A. Selloni, Electronic structure and bonding properties of cobalt oxide in the spinel structure, *Phys. Rev. B* **83**, 245204 (2011).
- [34] K. O. Obodo, C. N. M. Ouma, G. Gebreyesus, J. T. Obodo, S. O. Ezeonu, and B. Bouhafs, DFT + *U* studies of the electronic and optical properties of ReS₂ mono-layer doped with lanthanide atoms, *Mater. Res. Express* **6**, 106307 (2019).
- [35] Y. Wu, Y. Zhang, F. Du, B. Shen, H. Zheng, Y. Fang, M. Smidman, C. Cao, F. Steglich, H. Yuan, J. D. Denlinger, and Y. Liu, Anisotropic *c-f* hybridization in the ferromagnetic quantum critical metal CeRh₆Ge₄, *Phys. Rev. Lett.* **126**, 216406 (2021).
- [36] D. W. Tam, N. Colonna, F. Alarab, V. N. Strocov, D. J. Gawryluk, E. Pomjakushina, and M. Kenzelmann, Flat-band hybridization between *f* and *d* states near the Fermi energy of SmCoIn₅, *npj Quantum Mater.* **9**, 26 (2024).
- [37] A. Togo, L. Chaput, T. Tadano, and I. Tanaka, Implementation strategies in phonopy and phono3py, *J. Phys.: Condens. Matter* **35**, 353001 (2023).
- [38] Y. W. Cheung, J. Z. Zhang, J. Y. Zhu, W. C. Yu, Y. J. Hu, D. G. Wang, Y. Otomo, K. Iwasa, K. Kaneko, M. Imai, H. Kanagawa, K. Yoshimura, and S. K. Goh, Second-order structural transition in the superconductor La₃Co₄Sn₁₃, *Phys. Rev. B* **93**, 241112(R) (2016).
- [39] See Supplemental Material at <http://link.aps.org/supplemental/10.1103/PhysRevB.111.165119> for the inverse susceptibility vs temperature plot and Curie-Weiss fit of PCS, the temperature-dependent RIXS spectra acquired at the Co edge, and the phonon spectrum of PCS at 300 and 90 K along with the partial density of states of Pr, Co, and Sn at 300 and 90 K, respectively, and which includes Refs. [40–49].
- [40] K. P. K. Kumar, J. W. Chiou, H. M. Tsai, C. W. Pao, J. C. Jan, P. C. Hsu, D. C. Ling, F. Z. Chien, W. F. Pong, M.-H. Tsai *et al.*, Electronic and local atomic structures of (La_{1-x}Pr_x)_{0.85}Zr_{0.15}MnO₃ studied by x-ray absorption spectroscopy, *J. Phys.: Condens. Matter* **17**, 4197 (2005).
- [41] J. Keller, M. Castro, and C. Amador, Rare earths presenting strong *f-d* hybridization, *Physica B+C (Amsterdam)* **102**, 129 (1980).
- [42] A. Kotani and S. Shin, Resonant inelastic x-ray scattering spectra for electrons in solids, *Rev. Mod. Phys.* **73**, 203 (2001).
- [43] L. J. P. Ament, M. van Veenendaal, T. P. Devereaux, J. P. Hill, and J. van den Brink, Resonant inelastic x-ray scattering studies of elementary excitations, *Rev. Mod. Phys.* **83**, 705 (2011).
- [44] B. Liu, M. M. van Schooneveld, Y.-T. Cui, J. Miyawaki, T. O. Eschemann, K. P. de Jong, M. U. Delgado-Jaime, and F. M. F. de Groot, In-situ 2p3d resonant inelastic x-ray scattering tracking cobalt nanoparticle reduction, *J. Phys. Chem. C* **121**, 17450 (2017).
- [45] M. M. van Schooneveld, R. Kurian, A. Juhin, K. J. Zhou, J. Schlappa, V. N. Strocov, T. Schmitt, and F. M. F. de Groot, Electronic structure of CoO nanocrystals and a single crystal probed by resonant x-ray emission spectroscopy, *J. Phys. Chem. C* **116**, 15218 (2012).
- [46] A. R. Shelke, H.-T. Wang, J.-W. Chiou, I. Shown, A. Sabbah, K.-H. Chen, S.-A. Teng, I.-A. Lin, C.-C. Lee, H.-C. Hsueh *et al.*, Bandgap shrinkage and charge transfer in 2D layered SnS₂ doped with V for photocatalytic efficiency improvement, *Small* **18**, 2105076 (2021).
- [47] H. Y. Huang, A. Singh, C. I. Wu, J. D. Xie, J. Okamoto, A. A. Belik, E. Kurmaev, A. Fujimori, C. T. Chen, S. V. Streltsov *et al.*, Resonant inelastic x-ray scattering as a probe of *J_{eff}* = 1/2 state in 3d transition-metal oxide, *npj Quantum Mater.* **7**, 33 (2022).
- [48] T. Sudayama, K. Uehara, T. Mukai, D. Asakura, X.-M. Shi, A. Tsuchimoto, B. Mortemard de Boisse, T. Shimada, E. Watanabe, Y. Harada *et al.*, Multiorbital bond formation for stable oxygen-redox reaction in battery electrodes, *Energy Environ. Sci.* **13**, 1492 (2020).
- [49] A. Agui, T. Uozumi, M. Mizumaki, and T. Käämbre, Inter-metallic charge transfer in FeTiO₃ probed by resonant inelastic soft x-ray scattering, *Phys. Rev. B* **79**, 092402 (2009).
- [50] Y. Oduchi, C. Tonohiro, A. Thamizhavel, H. Nakashima, S. Morimoto, T. D. Matsuda, Y. Haga, K. Sugiyama, T. Takeuchi, R. Settai *et al.*, Magnetic properties of Ce₃T₄Sn₁₄ and Pr₃T₄Sn₁₃ (T = Co and Rh) single crystals, *J. Magn. Magn. Mater.* **310**, 249 (2007).
- [51] J. E. Van Vleck, *The Theory of Electric and Magnetic Susceptibilities* (Oxford University Press, London, 1932).

- [52] W. H. Bragg and W. L. Bragg, The reflection of x-rays by crystals, *Proc. R. Soc. London A* **88**, 428 (1913).
- [53] S. H. Hsieh, R. S. Solanki, Y. F. Wang, Y. C. Shao, S. H. Lee, C. H. Yao, C. H. Du, H. T. Wang, J. W. Chiou, Y. Y. Chin *et al.*, Anisotropy in the thermal hysteresis of resistivity and charge density wave nature of single crystal $\text{SrFeO}_{3-\delta}$: X-ray absorption and photoemission studies, *Sci. Rep.* **7**, 161 (2017).
- [54] B. Ravel and M. Newville, *ATHENA, ARTEMIS, HEPHAESTUS*: Data analysis for x-ray absorption spectroscopy using *IFEFFIT*, *J. Synchrotron Radiat.* **12**, 537 (2005).
- [55] H. T. Wang, Anirudha Ghosh, C. H. Wang, S. H. Hsieh, Y. C. Shao, J. W. Chiou, C. L. Chen, C. W. Pao, J. F. Lee, Y. S. Liu *et al.*, Evolution of superconductivity in $\text{K}_{2-x}\text{Fe}_{4+y}\text{Se}_5$: Spectroscopic studies of x-ray absorption and emission, *Proc. Natl. Acad. Sci. USA* **116**, 22458 (2019).
- [56] R. H. Petrucci, F. G. Herring, J. D. Madura, and C. Bissonnette, *General Chemistry: Principles and Modern Applications* (Pearsons, Essex, 2017).
- [57] G. Sarret, E. A. H. P. Smits, H. C. Michel, M. P. Isaure, F. J. Zhao, and R. Tappero, *Advances in Agronomy*, edited by D. L. Sparks (Academic, New York, 2013), Vol. 119, Chap. 1.
- [58] A. Pal, S. Ghosh, A. G. Joshi, S. Kumar, S. Patil, P. K. Gupta, P. Singh, V. K. Gangwar, P. Prakash, R. K. Singh *et al.*, Investigation of multi-mode spin-phonon coupling and local B-site disorder in $\text{Pr}_2\text{CoFeO}_6$ by Raman spectroscopy and correlation with its electronic structure by XPS and XAS studies, *J. Phys.: Condens. Matter* **31**, 275802 (2019).
- [59] G. Ghiringhelli, M. Matsubara, C. Dallera, F. Fracassi, R. Gusmeroli, A. Piazzalunga, A. Tagliaferri, N. B. Brookes, A. Kotani, and L. Braicovich, NiO as a test case for high resolution resonant inelastic soft x-ray scattering, *J. Phys.: Condens. Matter* **17**, 5397 (2005).
- [60] W. A. Harrison, *Electronic Structure and the Properties of Solids* (Freeman, San Francisco, 1980).
- [61] R. Huisman, R. de Jonge, C. Haas, and F. Jellinek, Trigonal-prismatic coordination in solid compounds of transition metals, *J. Solid State Chem.* **3**, 56 (1971).
- [62] *Martensitic Transformations*, edited by S. Banerjee and P. Mukhopadhyay, Pergamon Materials Series (Pergamon, New York, 2007), Vol. 12, Chap. 4, p. 257.
- [63] P. Gao, R. Li, Y. Liu, G. Chen, M. Zhu, Y. Jian, Z. Wu, X. Lu, Y. Ren, and C. Li, In-situ synchrotron diffraction study of the localized phase transformation and deformation behavior in NiTi SMA, *Mater. Sci. Eng., A* **805**, 140560 (2021).
- [64] L. Cheng, C. Liang, X. Zou, Z. Liu, J. Wu, S. Zhang, and S. Qiao, Negative thermal expansion of the stars of David in a 1T'-NbSe₂ monolayer at about 50 K, *Phys. Rev. B* **108**, 214103 (2023).
- [65] H. Negishi, Y. Kuroiwa, H. Akamine, S. Aoyagi, A. Sawada, T. Shobu, S. Negishi, and M. Sasaki, CDW-induced negative thermal expansion in two-dimensional conductor $\eta\text{-Mo}_4\text{O}_{11}$, *Solid State Commun.* **125**, 45 (2003).
- [66] G. Henkelman, A. Arnaldsson, and H. Jónsson, A fast and robust algorithm for Bader decomposition of charge density, *Comput. Mater. Sci.* **36**, 354 (2006).
- [67] F. J. Di Salvo, D. E. Moncton, and V. J. Waszczak, Electronic properties and superlattice formation in the semimetal TiSe_2 , *Phys. Rev. B* **14**, 4321 (1976).
- [68] Y. Aoki, T. Namiki, S. Ohsaki, S. R. Saha, H. Sugawara, and H. Sato, Thermodynamical study on the heavy-fermion superconductor $\text{PrOs}_4\text{Sb}_{12}$: Evidence for field-induced phase transition, *J. Phys. Soc. Jpn.* **71**, 2098 (2002).
- [69] G. Seyfarth, J. P. Brison, M.-A. Méasson, D. Braithwaite, G. Lapertot, and J. Flouquet, Superconducting $\text{PrOs}_4\text{Sb}_{12}$: A thermal conductivity study, *Phys. Rev. Lett.* **97**, 236403 (2006).